ACSNANO
www.acsnano.org
ARTICLE

Achieving Ultrafast Hole Transfer at the Monolayer MoS_2 and $CH_3NH_3PbI_3$ Perovskite Interface by Defect Engineering

Bo Peng,[†,‡,#] Guannan Yu,[§,#] Yawen Zhao,[∥,#] Qiang Xu,[§] Guichuan Xing,[§] Xinfeng Liu,[§,⊥] Deyi Fu,[†] Bo Liu,[†] Jun Rong Sherman Tan,[†] Wei Tang,[†] Haipeng Lu,[‡] Jianliang Xie,[‡] Longjiang Deng,[‡] Tze Chien Sum,*[,§] and Kian Ping Loh*[,†]

[†]Department of Chemistry and Centre for Advanced 2D Materials and Graphene Research Centre, National University of Singapore, 3 Science Drive 3, Singapore 117543, Singapore

[‡]National Engineering Research Center of Electromagnetic Radiation Control Materials and State Key Laboratory of Electronic Thin Films and Integrated Devices, University of Electronic Science and Technology of China, Chengdu 610054, China

[§]School of Physical & Mathematical Sciences, Nanyang Technological University, 21 Nanyang Link, Singapore 637371, Singapore

[⊥]CAS Center for Excellence in Nanoscience & CAS Key Laboratory of Standardization and Measurement for Nanotechnology, National Center for Nanoscience and Technology, Beijing 100190, China

[∥]China Academy of Engineering Physics, P.O. Box 919-71, Mianyang, 621900, Sichuan, China

Supporting Information

ABSTRACT: **The performance of a photovoltaic device is strongly dependent on the light harvesting properties of the absorber layer as well as the charge separation at the donor/acceptor interfaces. Atomically thin two-dimensional transition metal dichalcogenides (2-D TMDCs) exhibit strong light−matter interaction, large optical conductivity, and high electron mobility; thus they can be highly promising materials for next-generation ultrathin solar cells and optoelectronics. However, the short optical absorption path inherent in such atomically thin layers limits practical applications. A heterostructure geometry comprising 2-D TMDCs (*e.g.*, MoS_2) and a strongly absorbing material with long electron−hole diffusion lengths such as methylammonium lead halide perovskites ($CH_3NH_3PbI_3$) may overcome this constraint to some extent, provided the charge transfer at the heterostructure interface is not hampered by their band offsets. Herein, we demonstrate that the intrinsic band offset at the $CH_3NH_3PbI_3/MoS_2$ interface can be overcome by creating sulfur vacancies in MoS_2 using a mild plasma treatment; ultrafast hole transfer from $CH_3NH_3PbI_3$ to MoS_2 occurs within 320 fs with 83% efficiency following photoexcitation. Importantly, our work highlights the feasibility of applying defect-engineered 2-D TMDCs as charge-extraction layers in perovskite-based optoelectronic devices.**

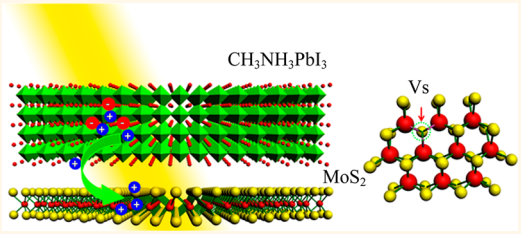

KEYWORDS: *perovskite, S vacancies, charge transfer, two-dimensional transition metal dichalcogenides, heterojunction*

Hybrid organic−inorganic methylammonium lead halide perovskite materials have attracted intense interest recently because of their alluring prospects as high-efficiency, low-cost solar cells.[1−3] To date, efficiencies of such solar cells have exceeded 22%.[4−9] $CH_3NH_3PbX_3$ perovskites exhibit strong solar absorption, long electron−hole diffusion lengths,[7−9] and relatively low trap densities for a solution-processed system,[10] which impart the following advantages: (1) the use of thinner layers for light harvesting, (2) efficient transfer of photoinduced charges to the heterointerface before recombination, and (3) low trapping losses. Previous reports have shown that photoinduced electrons in $CH_3NH_3PbI_3$ perovskite films were injected into TiO_2.[9,11] Marchioro and co-workers have shown that charge separation and injection take place simultaneously within the femtosecond-to-picosecond time scale at both the $CH_3NH_3PbI_3/TiO_2$ and $CH_3NH_3PbI_3$/spiro-OMeTAD interfaces.[12,13] Contrary to the low-cost benefit of perovskite solar cells, spiro-OMeTAD (a hole-transporting material (HTM)) is in fact more costly than gold in weight. Being organic in nature, the stability issue is another concern. Hence there are ongoing efforts to develop inorganic HTMs or to use new photovoltaic architectures that bypass the need for HTM.

Received: April 29, 2016
Accepted: May 31, 2016
Published: May 31, 2016

DOI: 10.1021/acsnano.6b02845
ACS Nano 2016, 10, 6383−6391

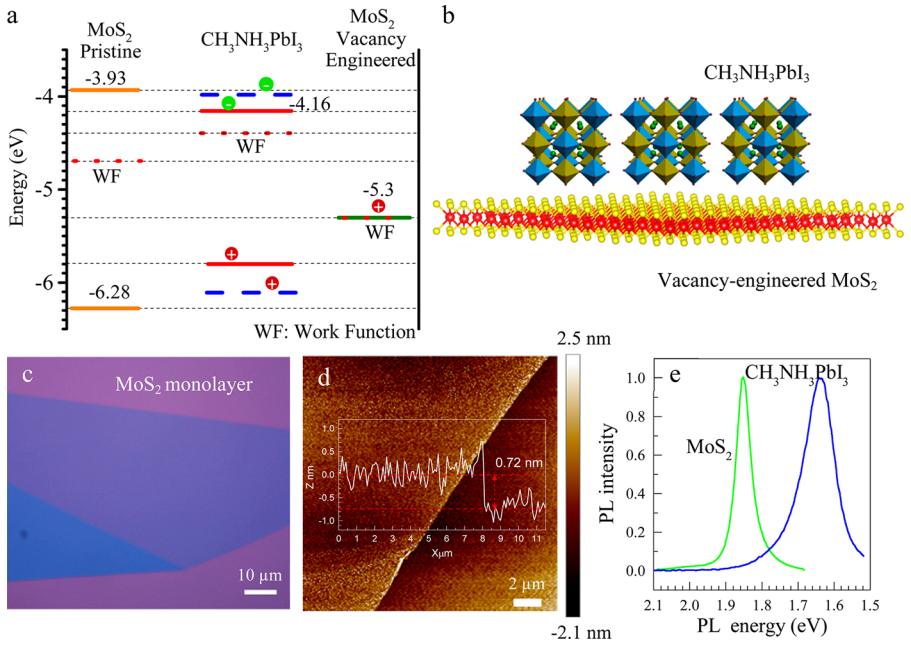

Figure 1. (a) Schematic of the band alignment of a pristine and vacancy-engineered MoS_2 monolayer and $CH_3NH_3PbI_3$. (b) Illustration of a vacancy-engineered $MoS_2/CH_3NH_3PbI_3$ heterostructure. (c) Microscope image of a ~100 μm MoS_2 monolayer on a SiO_2/Si substrate. (d) AFM image of monolayer MoS_2 on a SiO_2/Si substrate. The inset shows that the thickness is ~0.72 nm. (e) Typical PL spectra of a mechanically exfoliated MoS_2 monolayer flake and $CH_3NH_3PbI_3$ perovskite films.

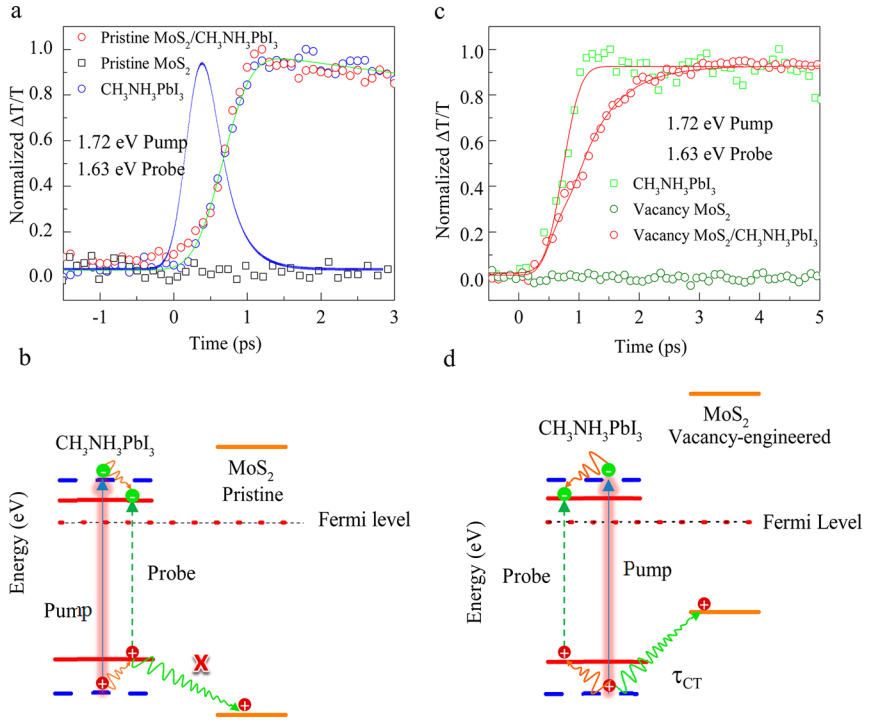

Figure 2. (a) Transient absorption signals at 1.63 eV upon excitation at 1.72 eV with a fluence of 6 μJ cm^{-2}. The invariance of the photobleach rise times indicates the absence of charge transfer between the pristine MoS_2 monolayer and $CH_3NH_3PbI_3$. The blue dashed line is the pump−probe laser cross-correlation of our spatially resolved micro pump−probe setup, which is found to be ~250 ± 40 fs. (b) Schematic illustrating the type I band alignment and the absence of charge transfer between the pristine MoS_2 monolayer and $CH_3NH_3PbI_3$. (c) Evolution of the photobleaching signals at 1.63 eV after excitation at 1.72 eV with a fluence of 7.2 μJ cm^{-2}. The increasing rise time indicates that the hole transfer take place. (d) Schematic of the type II energy alignment at the vacancy-engineered $MoS_2/CH_3NH_3PbI_3$ heterostructure favoring hole transfer from $CH_3NH_3PbI_3$ to the vacancy-engineered MoS_2 monolayer.

MoS_2 films are potentially good hole-transporting layers.[14−23] State-filling in MoS_2 occurs within 50 fs, and ultrafast charge transfer can also take place within the same time scale.[24−28] Solution-processed 2H-MoS_2 flakes have been used as hole transport layers in P3HT:$PC_{61}BM$ organic solar cells, showing better performance than PEDOT:PSS.[29,30] The

DOI: 10.1021/acsnano.6b02845
ACS Nano 2016, 10, 6383−6391

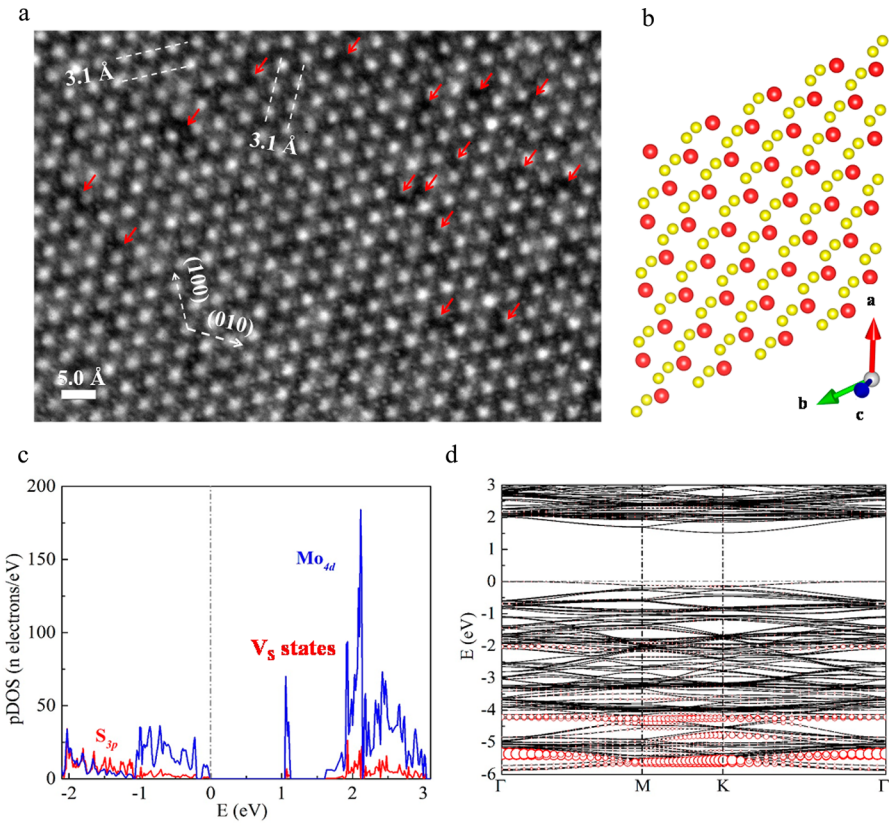

Figure 3. (a) Atomic structures of 1H phase monolayer MoS_2 with plasma treatment measured by aberration-corrected HRTEM. The monolayer MoS_2 is tilted by ~15° along the *c*-axis. The small S atoms and big Mo atoms are clearly distinguishable. The S vacancies (*Vs*) are highlighted by red arrows. (b) Illustration of corresponding monolayer MoS_2 in top view. The red and yellow spheres represent the Mo and S atoms. (c) Projected density of states (pDOS) of monolayer MoS_2 with a S-vacancy. The V_s defect states are introduced into the band, resulting in p-doping. (d) Projected band structure of monolayer MoS_2 with O_S defect.

selection of hole-transporting layer is based on the following principles: band alignment, atmosphere stability, transparency, and hole mobility. However, the interface physics of two-dimensional transition metal dichalcogenides (2-D TMDCs) with halide perovskites is not well understood. According to band edge analysis using ultraviolet photoelectron spectroscopy (UPS, Supplementary Figure S1), the valence band maximum (VBM) of $CH_3NH_3PbI_3$ perovskite films is at −5.79 eV, higher than the VBM of MoS_2 monolayer (−6.28 eV); thus a pristine MoS_2 monolayer and $CH_3NH_3PbI_3$ form a type I heterojunction (Figure 1a), which hampers the dissociation and transfer of photogenerated electrons and holes from $CH_3NH_3PbI_3$ to MoS_2. This raises the fundamental question of how to fabricate a type II interface in the 2-D MoS_2/$CH_3NH_3PbI_3$ heterostructure. Interestingly, we found that creating S vacancies in MoS_2 through mild O_2 plasma treatment strongly improves the hole transfer rate between $CH_3NH_3PbI_3$ and MoS_2. Our work underlines the importance of defect engineering in tuning the band alignment of MoS_2 in heterostructures.[31−34]

RESULTS AND DISCUSSION

Ultrafast Hole Transfer from $CH_3NH_3PbI_3$ Perovskite to a Vacancy-Engineered MoS_2 Monolayer. In order to verify the occurrence of ultrafast charge transfer at the MoS_2/perovskite interface, transient absorption spectroscopy (TAS) was performed to compare the dynamics at the MoS_2/$CH_3NH_3PbI_3$ and vacancy-engineered MoS_2/$CH_3NH_3PbI_3$ heterojunctions. Briefly, the "pump−probe" technique is based on using a pump pulse to first excite the carriers at the MoS_2/$CH_3NH_3PbI_3$ interface and then using a time-delayed probe pulse to interrogate the occupancy of these carriers at the valence or conduction bands by monitoring the absorption changes. Here, we monitor the photobleaching peaks (or $+\Delta T/T$ peaks from a reduction in absorption) of the direct gap transition from the valence band maximum to the conduction band minimum (CBM) of $CH_3NH_3PbI_3$, which give rise to a photobleaching peak located at ~1.63 eV (or ~760 nm).[35] Spatially resolved (or micro-area) transient absorption measurements were performed on the heterojunction and its nearby region with only $CH_3NH_3PbI_3$ (*i.e.*, as the control without MoS_2). The MoS_2/$CH_3NH_3PbI_3$ heterostructure was prepared by spin-coating a ~30 nm thickness $CH_3NH_3PbI_3$ layer on the MoS_2 monolayer flake (Figure 1b and Supplementary S2). MoS_2 monolayers were mechanically exfoliated from bulk crystal and transferred onto clear quartz treated by a mild O_2 plasma process. Figure 1c shows the microscope image of a ~100 μm MoS_2 monolayer on a SiO_2/Si substrate. The AFM image indicates the thickness of monolayer MoS_2 is ~0.72 nm (Figure 1d), which is closed to the interlayer distance of ~0.65 nm.[36] A very strong photoluminescence (PL) peak of MoS_2 at ~1.85 eV is detected upon optical excitation at 2.33 eV with a power of 0.1 mW, which is characteristic of the typical MoS_2 A-exciton resonances, and the strong PL of $CH_3NH_3PbI_3$ films is at ~1.63 eV (Figure 1e). Figure 2a shows the buildup of the normalized photobleaching signature from

DOI: 10.1021/acsnano.6b02845
ACS Nano 2016, 10, 6383−6391

the 1.63 eV peak for both the $CH_3NH_3PbI_3$ control (without MoS_2) and the pristine $MoS_2/CH_3NH_3PbI_3$ heterostructure, following ~1.72 eV (or ~720 nm) pump excitation to selectively excite $CH_3NH_3PbI_3$ only. This rise of the photobleaching transients reflects the state-filling at the perovskite band edges. A delayed rise time is indicative of charge extraction of the carriers prior to them relaxing to the band edges. However, the near invariance of the rise times signifies the absence of any such charge transfer, which is consistent with a type I band alignment between pristine MoS_2 and $CH_3NH_3PbI_3$ (Figure 2b). The rise time for both the $CH_3NH_3PbI_3$ control sample and the pristine $MoS_2/CH_3NH_3PbI_3$ heterostructure are 260 ± 50 and 260 ± 40 fs, respectively (Figure 2a and Supplementary S3) after deconvolving the instrument response function. In contrast, the photobleaching signatures for the vacancy-engineered $MoS_2/CH_3NH_3PbI_3$ heterostructures (Figure 2c) show a delayed rise as compared to the $CH_3NH_3PbI_3$-only film, which is indicative of charge transfer to MoS_2 in the former. When the photoinduced holes in $CH_3NH_3PbI_3$ are transferred into the vacancy-engineered MoS_2 monolayer, the band edge state-filling in perovskite becomes slower. The observed dynamical behavior (of longer PB rise time) in the vacancy-engineered $MoS_2/CH_3NH_3PbI_3$ is analogous to that in a previous report,[37] although the detailed mechanisms of the hole transfer in these cases are different. This would be consistent with a type II energy alignment at the vacancy-engineered $MoS_2/CH_3NH_3PbI_3$ heterostructure (Figure 2d). Similarly, the rise times of the $CH_3NH_3PbI_3$ control and the vacancy-engineered $MoS_2/CH_3NH_3PbI_3$ heterostructures were fitted to be 265 ± 40 and 580 ± 50 fs after deconvolving the instrument response function (red circles with the fitted red solid line in Figure 2c and Supplementary S3). Using a simple phenomenological model given by $k_{Relax1} = k_{Relax2} + k_{CT}$, where k_{Relax1} and k_{Relax2} are the hot hole cooling rates of $CH_3NH_3PbI_3$ in $CH_3NH_3PbI_3$-only films and the vacancy-engineered $MoS_2/CH_3NH_3PbI_3$ heterostructure, respectively, and k_{CT} is the hole transfer rate from $CH_3NH_3PbI_3$ to vacancy-engineered MoS_2 (see Supplementary S4 for details), we can estimate the hole transfer time τ_{CT} from $CH_3NH_3PbI_3$ to vacancy-engineered MoS_2 in the heterostructure using $1/\tau_{Relax1} = 1/\tau_{Relax2} + 1/\tau_{CT}$. Accordingly, τ_{CT} is estimated to be ~490 ± 50 fs (see Supplementary S4 for details). The hole transfer efficiency can be determined using the equation $\eta = k_{CT}/(k_{Relax2} + k_{CT})$ and is estimated to be ~54.1%. Importantly, the results here show clearly that defect engineering can overcome the band offset limitation in the $MoS_2/CH_3NH_3PbI_3$ heterostructure. This opens up a facile approach for tuning the hole transfer dynamics at the $MoS_2/CH_3NH_3PbI_3$ interface, which will be elaborated in the following paragraphs.

S-Vacancy-Engineered MoS_2 Monolayer. To directly observe the atomistic origin of the defect engineering, high-resolution TEM was applied to observe the type of defects generated following plasma treatment. The plasma-treated samples were transferred onto TEM grids using PMMA and then washed in acetone to remove the PMMA. Aberration-corrected high-resolution transmission electron microscopy (AC-HRTEM) was carried out to record images that are slightly underfocused. Figure 3a shows the AC-HRTEM image of the sample. It should be noted that the monolayer MoS_2 is tilted by ~15° in the *c*-axis. The lattice constant is $a = b = ~3.1$ Å, which is assigned to the (100) and (010) planes of monolayer MoS_2. The contrast between the Mo and S atoms is clearly detectable, and the small and big spheres represent S and Mo atoms, respectively. Two S atoms are found between three adjacent Mo atoms in the *a*- and *b*-axis, and the lattice structure agrees with the 1H phase (D_{3h}) of monolayer MoS_2. Figure 3b shows the top view of corresponding schematics of monolayer MoS_2 tilted by ~15° in the *c*-axis, and the positions of S and Mo atoms are in good agreement with those in the AC-HRTEM images. Importantly, many S atoms are removed by plasma treatment, resulting in S vacancy defects around the Mo atoms, which are highlighted by red arrows in Figure 3a. The S vacancies are found to diffuse, resulting in triangular vacancy clusters.[34,38] Defect agglomerations are further formed as the S vacancy concentration increases,[39] leading to significant lattice distortions (Supplementary S5, Figure S5). It should be noted that AC-HRTEM measurements do not offer any detectable signals of the MoO_3 domain in the monolayer MoS_2 with mild plasma treatment. In order to understand how S vacancies improve the hole transfer rate, first-principles calculation was carried out using the all-electron-like projector augmented wave (PAW) method[40] and the Perdew–Burke–Ernserhof (PBE) exchange–correlation potential,[41] which are implemented in the Vienna Ab-initio Simulation Package (VASP) (Supplementary S6).[42] The defect formation energies, ΔH_f (O_s, q), determine the type of predominant defect in monolayer MoS_2, which is defined as

$$\Delta H_f(O_s, q) = \Delta E(O_s, q) + n_S\mu_S + n_O\mu_O + qE_f \quad (1)$$

$$\Delta E(O_s, q) = E(O_s, q) - E(MoS_2) + n_S\mu^0{}_S + n_O\mu^0{}_O + qE_V \quad (2)$$

Here, $E(\alpha, q)$ is the total energy for the system containing the relaxed defect O atom, $E(MoS_2)$ is the total energy for the same supercell in the absence of the defect, and E_f is Fermi energy of the electrons referenced to the VBM of MoS_2 (E_V). μ_i is the chemical potential of constituent i referenced to elemental solid or gas with chemical potential $\mu^0{}_i$. The n_i are the number of S atoms, extrinsic defects O, and the number of electrons q transferred from the host to the reservoirs in forming the defect MoS_2. The calculated results show that the defect formation energy, $\Delta H_f(\alpha, 0)$, of the S vacancy (V_S) is 1.33 and 2.73 eV under S-poor and S-rich conditions, which is smaller than those of other intrinsic defects, *i.e.*, Mo vacancy (V_{Mo}, 7.2 and 4.4 eV), S antisite (S_{Mo}, 8.4 and 4.2 eV), and Mo antisite (Mo_S, 4.5 and 8.7 eV) (Supplementary S6, Table S1); therefore S vacancies are the main defect in monolayer MoS_2. The projected density of states (pDOS) of monolayer MoS_2 with a V_S defect is shown in Figure 3c. The defect level of V_S is mainly dominated by Mo_{4d} states lightly mixed with S_{3p} states. The V_S level is above the Fermi level, indicating that an acceptor energy level is introduced in the band gap. Thus, the V_S defect results in p-type doping in monolayer MoS_2.[31,38] The lowering of the Fermi level to the VBM increases the work function of the MoS_2 monolayer, which contributes to the breakthrough of band offset at the $MoS_2/CH_3NH_3PbI_3$ interface.

To understand the role of the oxygen defect, if any, in facilitating the charge transfer, we also calculated monolayer MoS_2 doped with O atoms, since the latter are present in the gas phase of our plasma environment.[43,44] In the monolayer MoS_2 supercell, we consider two doping cases, *i.e.*, one based on the substitutional doping of an S atom by O (O_S) and other based on the adsorption of an O atom on the sulfur site (O_{ads}). The results show that although the band gap decreases as the O

DOI: 10.1021/acsnano.6b02845
ACS Nano 2016, 10, 6383–6391

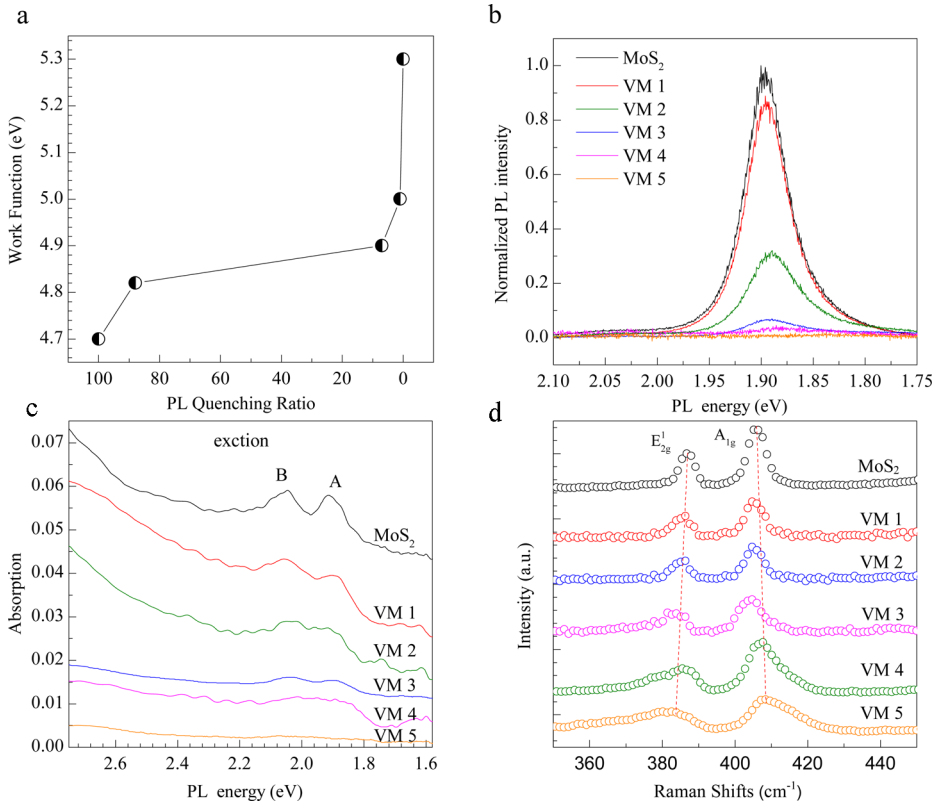

Figure 4. (a) Work function of a vacancy-engineered MoS_2 monolayer (VM) as a function of the PL quenching ratio, which is defined as the ratio of PL intensity after and before plasma treatment. The work function increases with increasing plasma power and time. (b, c, and d) The PL, absorption, and Raman spectra of an exfoliated MoS_2 monolayer and vacancy-engineered MoS_2 monolayer as a function of S vacancy concentration.

concentration increases,[32] the VBM hardly shifts. There is only a 0.05 eV downward shift of the VBM in the case of O_s doping and a 0.1 eV shift for the O_{ads} doping case (Supplementary S6, Figure S6). Therefore, the introduction of O atoms into monolayer MoS_2 does not influence the VBM and Fermi level. Figure 3d shows the projected band structure of O_S-doped monolayer MoS_2 with a band gap of 1.65 eV. The red circles represent the O component, where the size of the circle means the weight of O_{2p} states. It is found that the O_{2p} states are far below the VBM, which further confirms that O_S states do not contribute to the electron transition near the Fermi level and VBM. Therefore, our theoretical results suggest that S vacancies in the MoS_2 monolayer are the origin of the shifts in Fermi level following the plasma treatment, which leads to an improved band alignment at the interface, facilitating ultrafast hole transfer.

Scanning Kelvin probe microscopy (SKPM) was used to measure the work function of pristine and a vacancy-engineered MoS_2 monolayer.[45] The concentration of S vacancies can be increased by raising the plasma power and reaction time.[46] Consequently, the work function is increased due to the lowering of the Fermi level.[31,47] Figure 4a shows that the work function of vacancy-engineered MoS_2 can be engineered between 4.7 and 5.3 eV by varying the concentration of the S vacancies, which is consistent with our first-principles calculation results. It is worth pointing out that AFM studies show that the topography of the MoS_2 monolayer is almost indistinguishable before and after mild plasma treatment (Supplementary Figure S7). The photoluminescence feature peak of monolayer MoS_2 is at ~1.85 eV, which is characteristic of A-exciton resonances. The PL intensity of the MoS_2 monolayer gradually decreases with increasing plasma treatment power (Figure 4b) and eventually became completely quenched. The peak intensity of A-exciton and B-exciton transitions at ~1.9 and 2.05 eV decreases drastically (Figure 4c). We suggest that increasing the plasma power leads to the increasing concentration of S vacancies and other types of dislocations in the MoS_2 monolayer, which leads to a decrease in the exciton absorption intensity.[48,49] Meanwhile, the nonradiative rate of electron−hole recombination increases, resulting in the gradual PL quenching of the vacancy-engineered MoS_2 monolayer.[50] The Raman in-plane E_{2g}^1 mode and out-of-plane A_{1g} mode of an exfoliated MoS_2 monolayer are at 386.7 and 405.1 cm^{-1} (Figure 4d),[51−53] respectively. The creation of S vacancies in the MoS_2 lattice results in the softening of the out-of-plane A_{1g} vibration mode and stiffening of the in-plane E_{2g}^1 vibration mode; thus the A_{1g} peak red-shifts and the E_{2g}^1 peak blue-shifts. Significant disorders are generated in the lattice, leading to the increase in FWHM of the A_{1g} and E_{2g}^1 peaks.

Tuning of Ultrafast Hole Transfer Rate. To further validate our hole transfer model, we also photoexcite the vacancy-engineered $MoS_2/CH_3NH_3PbI_3$ at a higher energy of 2.48 eV, where a longer charge transfer time is expected due to holes cascading/transferring from deeper valence states. A detailed comparison of the photobleaching transients at the 1.63 eV photobleach peak following 2.48 eV excitation with a fluence of 6 μJ cm^{-2} for both the vacancy-engineered $MoS_2/CH_3NH_3PbI_3$ and $CH_3NH_3PbI_3$-only film was carried out (Figure 5a and Supplementary S8). Although in this case, both

DOI: 10.1021/acsnano.6b02845
ACS Nano 2016, 10, 6383−6391

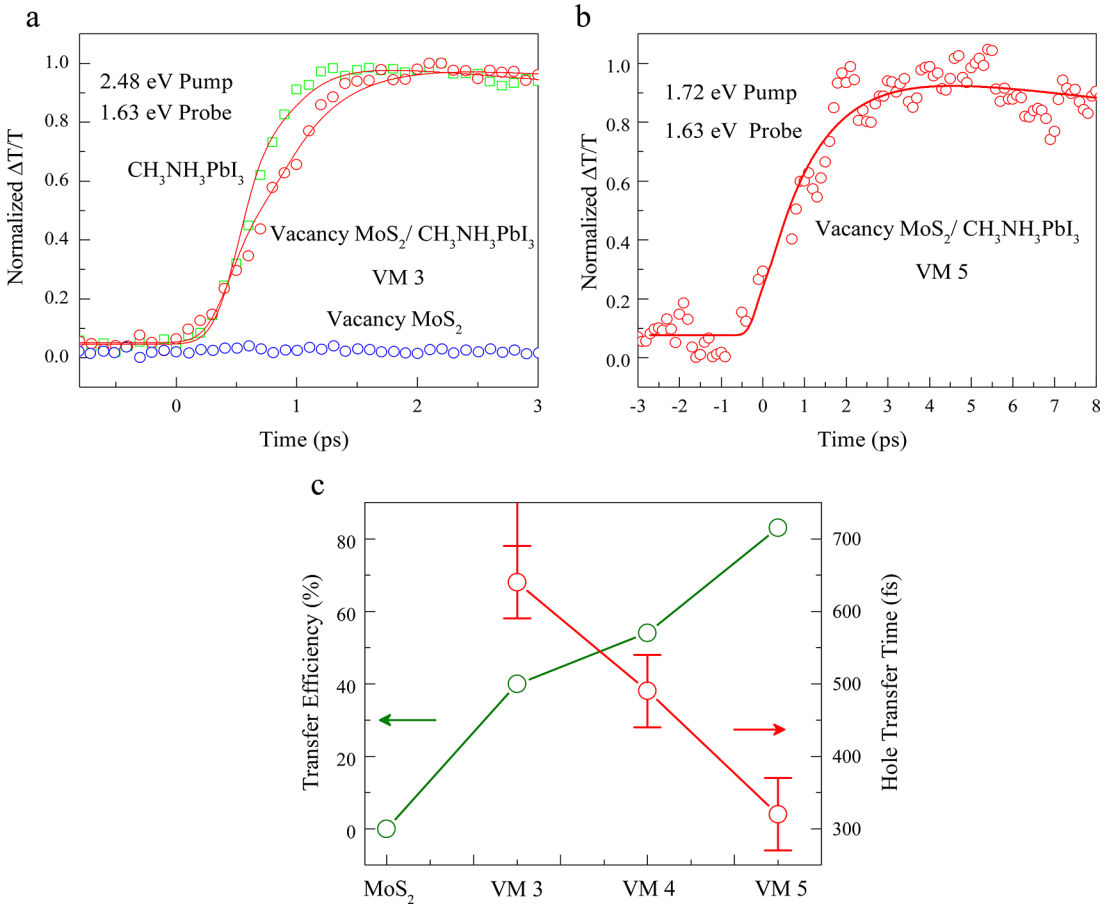

Figure 5. (a) Photobleaching signals at 1.63 eV after excitation at 2.48 eV with a fluence of 6 μJ cm^{-2} in $CH_3NH_3PbI_3$, vacancy-engineered MoS_2/$CH_3NH_3PbI_3$ heterostructure, and vacancy-engineered MoS_2 monolayer; see Figure 4 (VM 3). (b) Evolution of the photobleaching signals at 1.63 eV after excitation at 1.72 eV with a fluence of 7.2 μJ cm^{-2} as the bleach builds up. Prolonged oxygen plasma treatment of the MoS_2 flake resulted in the quenching of the PL; see Figure 4 (VM 5). (c) Hole transfer efficiency and time as a function of S vacancy density. The higher S vacancy density results in a higher hole transfer rate and efficiency.

the vacancy-engineered MoS_2 and $CH_3NH_3PbI_3$ can be excited, the photobleach signature is mainly from the perovskite, as the transient absorption signals from the vacancy-engineered MoS_2 alone are below the detection limit of our setup (blue circles in Figure 5a). By deconvoluting the instrument response function, the rise time of the 1.63 eV photobleach transient in the $CH_3NH_3PbI_3$ sample and vacancy-engineered MoS_2/$CH_3NH_3PbI_3$ heterostructures are estimated to be 270 ± 40 and 450 ± 50 fs, respectively (Figure 5a). The charge transfer time and efficiency are estimated to be ∼675 ± 50 fs and ∼40%, respectively. Indeed, photoexcitation at 2.48 eV results in a delayed transfer as expected. These transient absorption measurements unambiguously validate the ultrafast hole transfer from $CH_3NH_3PbI_3$ to the vacancy-engineered MoS_2 monolayer.

The charge transfer rate is determined by the expression $1/\tau_{CT} = cN_h$, where c (cm^3/s) is the hole-capture coefficient and N_h is the concentration of S vacancies in the vacancy-engineered MoS_2 monolayer.[37,54] Thus, the hole transfer rate between vacancy-engineered MoS_2 and $CH_3NH_3PbI_3$ can be tuned by adjusting the concentration of S vacancies in the MoS_2 monolayer *via* increasing the treatment time of mild plasma. A pump beam at 1.72 eV with a fluence of 7.2 μJ cm^{-2} is used to selectively photoexcite $CH_3NH_3PbI_3$ only. Using the same instrument response function for time convolution, the rise time of photobleaching transients at 1.63 eV in a heterostructure consisting of vacancy-engineered MoS_2 with more treatment time (VM 5) and $CH_3NH_3PbI_3$ is estimated to be 1.56 ± 0.06 ps (Figure 5b). Accordingly, the charge transfer time is significantly improved to ∼320 ± 50 fs, and the hole transfer efficiency is increased to ∼83%. The hole transfer efficiency at the vacancy-engineered MoS_2 monolayer/$CH_3NH_3PbI_3$ interface is comparable with that of the reported hole injection efficiency from $CH_3NH_3PbI_3$ to spiro-OMeTAD (90 nm thickness),[7,12,55] which occurs within picoseconds following photoexcitation. This suggests that the vacancy-engineered MoS_2 monolayer is an excellent hole-transporting material and a promising alternative to spiro-OMeTAD in terms of its ultrathin, chemically and thermally stable, and highly efficient photovoltaic architecture. It should be noted that the hole transfer efficiency is 40%, 54%, and 83% with the increasing S vacancy concentration in the vacancy-engineered MoS_2 monolayer (VM 3, VM 4, VM 5), while the hole transfer times are 675 ± 50, 490 ± 50, and 320 ± 50 fs, respectively, as shown in Figure 5c. Thus, our results suggest that the hole transfer efficiency increases with the increasing population of S vacancies in the vacancy-engineered MoS_2 monolayer.

CONCLUSION

Our charge transfer dynamics studies reveal that holes can be efficiently transferred at the heterointerface of a vacancy-engineered MoS_2 monolayer and $CH_3NH_3PbI_3$, but not at the

DOI: 10.1021/acsnano.6b02845
ACS Nano 2016, 10, 6383−6391

interface comprising pristine monolayer MoS_2. The formation of S vacancies in the MoS_2 monolayer p-dopes the material and facilitates ultrafast hole transfer from $CH_3NH_3PbI_3$ to MoS_2. A viable strategy to tune the hole transfer dynamics is based on controlling the population of S vacancies, where a higher population leads to higher charge transfer efficiency. Vacancy-engineered $MoS_2/CH_3NH_3PbI_3$ heterostructures exhibit ultrafast hole transfer dynamics within the hundreds of femtoseconds time scale, suggesting that the vacancy-engineered MoS_2 monolayer and $CH_3NH_3PbI_3$ can be incorporated as an ultrathin hole extraction layer and active layer in optoelectronic devices.[56] Recent developments in the large-scale preparation of MoS_2 by CVD will allow the integration of a vacancy-engineered MoS_2 monolayer as a cost-effective ultrathin hole transport layer in large-area perovskite solar cells.[51,57−60]

The poor stability of lead halide perovskite solar cells in air has so far hampered sustained operation under normal conditions;[61] thus addressing the long-term stability is critical for future developments. The perovskite photoactive layer can be protected by using stable inorganic hole transport layers (CuSCN, CuI, NiO_x, and Ni_xMg_yO).[62−65] Using partially oxidized 2H-phase MoS_2 nanosheets (MoO_3−MoS_2) as hole-transporting material, long-term performance and stability have been achieved in organic solar cells (MoO_3−MoS_2/P3HT:$PC_{61}BM$/Al).[29] Therefore, it is possible that a MoS_2 monolayer, besides serving as a hole transport layer, can also act as an excellent protective layer to protect the perovskite from moisture and air.

METHODS

CH_3NH_3I Synthesis. CH_3NH_3I was synthesized by using a reported method.[66] Briefly, 3.04 mL of methylamine (40% in methanol, TCI) was added in 50 mL of ethanol under Ar gas, and the solution was stirred for 30 min at 0 °C. Then, 2 mL of hydroiodic acid (55 wt % in water, Sigma-Aldrich) was added. The mixed solutions were further stirred for 2 h. The white raw product methylammonium iodide (CH_3NH_3I) was obtained by rotary evaporation at 50 °C, washed three times with diethyl ether, and then finally recrystallized from a mixed solvent of diethyl ether and ethanol. The white solid was dried under vacuum for 24 h and stored in a glovebox.

$MoS_2/CH_3NH_3PbI_3$ Heterostructure Preparation. MoS_2 monolayer flakes were mechanically exfoliated from bulk crystal onto PDMS films and then transferred onto various substrates such as clear quartz, flat Au film, and Si/SiO_3 (300 nm) substrates. The MoS_2 monolayer was treated by a reactive ion etching system (VITA-MINI) to generate S vacancies (Supplementary S9). The 6.4 wt % solutions of PbI_2 and CH_3NH_3I in dimethylformamide were spin-coated on the MoS_2 samples, which were kept under vacuum for 1 h to remove the residual DMF solvent. $MoS_2/CH_3NH_3PbI_3$ heterostructures were stored in a glovebox before measurements.

Spatially Resolved (or Micro-area) Transient Absorption Spectroscopy. Spatially resolved transient absorption spectroscopy was performed in transmission mode driven by a femtosecond laser system seeded by a mode-locked Ti-sapphire oscillator (Coherent Vitesse, 80 MHz). The system output beam at 800 nm was generated through a 1 kHz regenerative amplifier (Coherent Libra) with a pulse width of 50 fs and a power of 4 mJ/pulse. Pump and probe beams were generated from two separate optical parametric amplifiers (OPerA Solo). Both beams were aligned and well overlapped coaxially to pass through the long working distance 100× objective lens (NA 0.7). Subsequently, the pump beam passing through the sample was filtered by a 775 ± 23 nm band-pass filter and a 740 nm long-pass filter, while the transmitted probe beam was detected by a photodiode and a lock-in amplifier after modulating the pump beam with a 83 Hz chopper.

Scanning Kelvin Probe Microscopy Measurement. SKPM was measured using a Park Systems XE-100 AFM. The exfoliated MoS_2 monolayer was first transferred onto flat Au substrates prepared by the procedures described in the literature[67] and then treated by mild O_2 plasma. The cantilevers with Au-coated tips used for the measurements were purchased from Mikromasch. The topographic and surface potential (SP) measurements were obtained using a dual-pass tapping mode with a cantilever resonant frequency of approximately 160 kHz. In the SKPM measurement, the Fermi levels are aligned between the electrically connected sample surface and the Au tip. The work function (WF) difference between the sample and tip will generate a field that will be nullified by the voltage applied from the SKPM system identified as the surface potential. The SP is defined as

$$SP = WF_{tip} - WF_{sample}$$

where WF_{tip} and WF_{sample} are the WFs of the conductive tip and the sample, respectively. In this study, the probe tip has been calibrated with highly ordered pyrolytic graphite (HOPG) (WF_{HOPG} = 4.6 eV) in order to convert the SP to the absolute work function of the sample as follows:

$$WF_{sample} = 4.6 + SP_{HOPG} - SP_{sample}$$

HRTEM Measurement. TEM imaging was carried out in an image aberration-corrected TEM (FEI Titan 80-300 operating at 60 kV), and a charge-coupled device camera (2*2 k, GatanUltraScan 1000) is used for image recording with an exposure time of 0.5 s. The third-order spherical aberration was set in the range 0.2−1 μm, and the TEM images were recorded slightly underfocused.

UV−Vis Absorption, PL, and Raman Measurement. UV−vis absorption data of pristine and vacancy-engineered MoS_2 monolayers were obtained by a CRAIC 20 UV−visible−NIR microspectrophotometer. The PL and Raman signals were record by a Witec Alpha 300R Plus confocal Raman microscope upon 532 nm laser excitation with 0.1 mW.

ASSOCIATED CONTENT

Supporting Information

The Supporting Information is available free of charge on the ACS Publications website at DOI: 10.1021/acsnano.6b02845.

Determination of band alignment in a $MoS_2/CH_3NH_3PbI_3$ heterostructure; thickness measurement of $CH_3NH_3PbI_3$ perovskite films; system response deconvolution; charge transfer modeling; triangular vacancy clusters and defect agglomerations; calculation method; topography images of MoS_2 monolayer before and after O_2 plasma; ultrafast hole transfer between vacancy-engineered MoS_2 monolayer and $CH_3NH_3PbI_3$ upon excitation at 2.48 eV; experimental parameters of mild O_2 plasma treatment on MoS_2 monolayer (PDF)

AUTHOR INFORMATION

Corresponding Authors

*Tel (T. C. Sum): (+65) 6316 2971. Fax: (+65) 6316 6984. E-mail: tzechien@ntu.edu.sg.

*Tel (K. P. Loh): (65)-6516-4402. Fax: (65)-6779-1691. E-mail: chmlohkp@nus.edu.sg.

Author Contributions

K.P.L. and T.C.S. conceived and supervised the experiment. B.P. synthesized $CH_3NH_3PbI_3$ perovskites and prepared the $MoS_2/CH_3NH_3PbI_3$ heterostructures. B.P., X.L., and G.Y. carried out pump−probe measurements. Q.X. did the calculations. B.P., B.L., and D.F. prepared the mechanically exfoliated monolayer MoS_2. J.S. carried out the UPS and SKPM measurement. Y.Z., J.X., L.D., and W.T. carried out the HRTEM measurement. B.P., G.Y., X.L., L.D., W.T., G.X.,

DOI: 10.1021/acsnano.6b02845
ACS Nano 2016, 10, 6383−6391

T.C.S., and K.P.L. performed data analysis. All authors discussed the results and wrote the manuscript.

Author Contributions

[#]B. Peng, G. Yu, and Y. Zhao contributed equally to this work.

Notes

The authors declare no competing financial interest.

ACKNOWLEDGMENTS

Funding from the Singapore National Research Foundation through the Singapore–Berkeley Research Initiative for Sustainable Energy (SinBeRISE) CREATE Program is gratefully acknowledged. K.P.L. thanks ARF Tier 1 Grant "2-D Crystals as Platform for Optoelectronics R-143-000-556-112" and A* star-DST project number 1425203139 "Flexible and high performance perovskite based solar cells on graphene electrodes". B.P. acknowledges financial support from ZYGX2015KYQD057 (A03013023601007). T.C.S. acknowledges the financial support from Nanyang Technological University start-up grant M4080514, the Ministry of Education Tier 1 grant RG101/15, and AcRF Tier 2 grants MOE2013-T2-1-081 and MOE2014-T2-1-044. We thank Prof. Qihua Xiong (SPMS, NTU) for his help on absorption studies of our samples.

REFERENCES

(1) Green, M. A.; Ho-Baillie, A.; Snaith, H. J. The Emergence of Perovskite Solar Cells. *Nat. Photonics* **2014**, *8*, 506–514.

(2) Im, J.-H.; Jang, I.-H.; Pellet, N.; Grätzel, M.; Park, N.-G. Growth of CH3NH3PbI3 Cuboids with Controlled Size for High-Efficiency Perovskite Solar Cells. *Nat. Nanotechnol.* **2014**, *9*, 927–932.

(3) Kojima, A.; Teshima, K.; Shirai, Y.; Miyasaka, T. Organometal Halide Perovskites as Visible-Light Sensitizers for Photovoltaic Cells. *J. Am. Chem. Soc.* **2009**, *131*, 6050–6051.

(4) Best Research-Cell Efficienies, http://www.nrel.gov/ncpv/, http://www.nrel.gov/ncpv/images/efficiency_chart.jpg. March 2016.

(5) Jeon, N. J.; Noh, J. H.; Yang, W. S.; Kim, Y. C.; Ryu, S.; Seo, J.; Seok, S. I. Compositional Engineering of Perovskite Materials for High-Performance Solar Cells. *Nature* **2015**, *517*, 476–480.

(6) Burschka, J.; Pellet, N.; Moon, S.-J.; Humphry-Baker, R.; Gao, P.; Nazeeruddin, M. K.; Gratzel, M. Sequential Deposition as a Route to High-Performance Perovskite-Sensitized Solar Cells. *Nature* **2013**, *499*, 316–319.

(7) Xing, G.; Mathews, N.; Sun, S.; Lim, S. S.; Lam, Y. M.; Grätzel, M.; Mhaisalkar, S.; Sum, T. C. Long-Range Balanced Electron- and Hole-Transport Lengths in Organic-Inorganic CH3NH3PbI3. *Science* **2013**, *342*, 344–347.

(8) Stranks, S. D.; Eperon, G. E.; Grancini, G.; Menelaou, C.; Alcocer, M. J. P.; Leijtens, T.; Herz, L. M.; Petrozza, A.; Snaith, H. J. Electron-Hole Diffusion Lengths Exceeding 1 Micrometer in an Organometal Trihalide Perovskite Absorber. *Science* **2013**, *342*, 341–344.

(9) Lee, M. M.; Teuscher, J.; Miyasaka, T.; Murakami, T. N.; Snaith, H. J. Efficient Hybrid Solar Cells Based on Meso-Superstructured Organometal Halide Perovskites. *Science* **2012**, *338*, 643–647.

(10) Xing, G.; Mathews, N.; Lim, S. S.; Yantara, N.; Liu, X.; Sabba, D.; Grätzel, M.; Mhaisalkar, S.; Sum, T. C. Low-Temperature Solution-Processed Wavelength-Tunable Perovskites for Lasing. *Nat. Mater.* **2014**, *13*, 476–480.

(11) Liu, M.; Johnston, M. B.; Snaith, H. J. Efficient Planar Heterojunction Perovskite Solar Cells by Vapour Deposition. *Nature* **2013**, *501*, 395–398.

(12) Marchioro, A.; Teuscher, J.; Friedrich, D.; Kunst, M.; van de Krol, R.; Moehl, T.; Gratzel, M.; Moser, J.-E. Unravelling the Mechanism of Photoinduced Charge Transfer Processes in Lead Iodide Perovskite Solar Cells. *Nat. Photonics* **2014**, *8*, 250–255.

(13) Ponseca, C. S.; Savenije, T. J.; Abdellah, M.; Zheng, K.; Yartsev, A.; Pascher, T.; Harlang, T.; Chabera, P.; Pullerits, T.; Stepanov, A.; et al. Organometal Halide Perovskite Solar Cell Materials Rationalized: Ultrafast Charge Generation, High and Microsecond-Long Balanced Mobilities, and Slow Recombination. *J. Am. Chem. Soc.* **2014**, *136*, 5189–5192.

(14) Britnell, L.; Ribeiro, R. M.; Eckmann, A.; Jalil, R.; Belle, B. D.; Mishchenko, A.; Kim, Y. J.; Gorbachev, R. V.; Georgiou, T.; Morozov, S. V.; et al. Strong Light-Matter Interactions in Heterostructures of Atomically Thin Films. *Science* **2013**, *340*, 1311–1314.

(15) Tsai, M. L.; Su, S. H.; Chang, J. K.; Tsai, D. S.; Chen, C. H.; Wu, C. I.; Li, L. J.; Chen, L. J.; He, J. H. Monolayer MoS2 Heterojunction Solar Cells. *ACS Nano* **2014**, *8*, 8317–8322.

(16) Bernardi, M.; Palummo, M.; Grossman, J. C. Extraordinary Sunlight Absorption and One Nanometer Thick Photovoltaics Using Two-Dimensional Monolayer Materials. *Nano Lett.* **2013**, *13*, 3664–3670.

(17) Feng, J.; Qian, X.; Huang, C.-W.; Li, J. Strain-Engineered Artificial Atom as a Broad-Spectrum Solar Energy Funnel. *Nat. Photonics* **2012**, *6*, 866–872.

(18) Kozawa, D.; Kumar, R.; Carvalho, A.; Kumar Amara, K.; Zhao, W.; Wang, S.; Toh, M.; Ribeiro, R. M.; Castro Neto, A. H.; Matsuda, K.; et al. Photocarrier Relaxation Pathway in Two-Dimensional Semiconducting Transition Metal Dichalcogenides. *Nat. Commun.* **2014**, *5*, 4543.

(19) Mak, K. F.; Lee, C.; Hone, J.; Shan, J.; Heinz, T. F. Atomically Thin MoS2: A New Direct-Gap Semiconductor. *Phys. Rev. Lett.* **2010**, *105*, 136805.

(20) Lee, C. H.; Lee, G. H.; van der Zande, A. M.; Chen, W.; Li, Y.; Han, M.; Cui, X.; Arefe, G.; Nuckolls, C.; Heinz, T. F.; et al. Atomically Thin P–N Junctions with Van Der Waals Heterointerfaces. *Nat. Nanotechnol.* **2014**, *9*, 676–681.

(21) Chhowalla, M.; Shin, H. S.; Eda, G.; Li, L. J.; Loh, K. P.; Zhang, H. The Chemistry of Two-Dimensional Layered Transition Metal Dichalcogenide Nanosheets. *Nat. Chem.* **2013**, *5*, 263–275.

(22) Furchi, M. M.; Pospischil, A.; Libisch, F.; Burgdörfer, J.; Mueller, T. Photovoltaic Effect in an Electrically Tunable Van Der Waals Heterojunction. *Nano Lett.* **2014**, *14*, 4785–4791.

(23) Peng, B.; Ang, P. K.; Loh, K. P. Two-Dimensional Dichalcogenides for Light-Harvesting Applications. *Nano Today* **2015**, *10*, 128–137.

(24) Hong, X.; Kim, J.; Shi, S.-F.; Zhang, Y.; Jin, C.; Sun, Y.; Tongay, S.; Wu, J.; Zhang, Y.; Wang, F. Ultrafast Charge Transfer in Atomically Thin MoS2/Ws2 Heterostructures. *Nat. Nanotechnol.* **2014**, *9*, 682–686.

(25) Ceballos, F.; Bellus, M. Z.; Chiu, H.-Y.; Zhao, H. Ultrafast Charge Separation and Indirect Exciton Formation in a MoS2–MoSe2 Van Der Waals Heterostructure. *ACS Nano* **2014**, *8*, 12717–12724.

(26) Komsa, H. P.; Krasheninnikov, A. V. Electronic Structures and Optical Properties of Realistic Transition Metal Dichalcogenide Heterostructures from First Principles. *Phys. Rev. B: Condens. Matter Mater. Phys.* **2013**, *88*, 085318.

(27) Terrones, H.; López Urías, F.; Terrones, M. Novel Hetero-Layered Materials with Tunable Direct Band Gaps by Sandwiching Different Metal Disulfides and Diselenides. *Sci. Rep.* **2013**, *3*, 1549.

(28) Peng, B.; Yu, G.; Liu, X.; Liu, B.; Liang, X.; Bi, L.; Deng, L.; Sum, T. C.; Loh, K. P. Ultrafast Charge Transfer in MoS2 /WSe2 P–N Heterojunction. *2D Mater.* **2016**, *3*, 025020.

(29) Yun, J. M.; Noh, Y. J.; Lee, C. H.; Na, S. I.; Lee, S.; Jo, S. M.; Joh, H. I.; Kim, D. Y. Exfoliated and Partially Oxidized MoS2 Nanosheets by One-Pot Reaction for Efficient and Stable Organic Solar Cells. *Small* **2014**, *10*, 2319–2324.

(30) Gu, X.; Cui, W.; Li, H.; Wu, Z.; Zeng, Z.; Lee, S. T.; Zhang, H.; Sun, B. A Solution-Processed Hole Extraction Layer Made from Ultrathin MoS2 Nanosheets for Efficient Organic Solar Cells. *Adv. Energy Mater.* **2013**, *3*, 1262–1268.

(31) Komsa, H.-P.; Krasheninnikov, A. V. Native Defects in Bulk and Monolayer MoS_2 from First Principles. *Phys. Rev. B: Condens. Matter Mater. Phys.* **2015**, *91*, 125304.

DOI: 10.1021/acsnano.6b02845
ACS Nano 2016, 10, 6383–6391

(32) KC, S.; Longo, R. C.; Wallace, R. M.; Cho, K. Surface Oxidation Energetics and Kinetics on MoS2Monolayer. *J. Appl. Phys.* **2015**, *117*, 135301.
(33) Sim, D. M.; Kim, M.; Yim, S.; Choi, M.-J.; Choi, J.; Yoo, S.; Jung, Y. S. Controlled Doping of Vacancy-Containing Few-Layer MoS2 *Via* Highly Stable Thiol-Based Molecular Chemisorption. *ACS Nano* **2015**, *9*, 12115−12123.
(34) Komsa, H.-P.; Kotakoski, J.; Kurasch, S.; Lehtinen, O.; Kaiser, U.; Krasheninnikov, A. V. Two-Dimensional Transition Metal Dichalcogenides under Electron Irradiation: Defect Production and Doping. *Phys. Rev. Lett.* **2012**, *109*, 035503.
(35) Sum, T. C.; Chen, S.; Xing, G.; Liu, X.; Wu, B. Energetics and Dynamics in Organic−Inorganic Halide Perovskite Photovoltaics and Light Emitters. *Nanotechnology* **2015**, *26*, 342001.
(36) Wang, Q. H.; KalantarZadeh, K.; Kis, A.; Coleman, J. N.; Strano, M. S. Electronics and Optoelectronics of Two-Dimensional Transition Metal Dichalcogenides. *Nat. Nanotechnol.* **2012**, *7*, 699−712.
(37) Li, M.; Xing, G.; Xing, G.; Wu, B.; Wu, T.; Zhang, X.; Sum, T. C. Origin of Green Emission and Charge Trapping Dynamics in Zno Nanowires. *Phys. Rev. B: Condens. Matter Mater. Phys.* **2013**, *87*, 115309.
(38) Qiu, H.; Xu, T.; Wang, Z.; Ren, W.; Nan, H.; Ni, Z.; Chen, Q.; Yuan, S.; Miao, F.; Song, F.; et al. Hopping Transport through Defect-Induced Localized States in Molybdenum Disulphide. *Nat. Commun.* **2013**, *4*, 2642.
(39) Komsa, H.-P.; Kurasch, S.; Lehtinen, O.; Kaiser, U.; Krasheninnikov, A. V. From Point to Extended Defects in Two-Dimensional MoS_2: Evolution of Atomic Structure under Electron Irradiation. *Phys. Rev. B: Condens. Matter Mater. Phys.* **2013**, *88*, 035301.
(40) Blöchl, P. E. Projector Augmented-Wave Method. *Phys. Rev. B: Condens. Matter Mater. Phys.* **1994**, *50*, 17953−17979.
(41) Perdew, J. P.; Burke, K.; Ernzerhof, M. Generalized Gradient Approximation Made Simple. *Phys. Rev. Lett.* **1996**, *77*, 3865−3868.
(42) Kresse, G.; Furthmüller, J. Efficient Iterative Schemes for Ab Initio Total-Energy Calculations Using a Plane-Wave Basis Set. *Phys. Rev. B: Condens. Matter Mater. Phys.* **1996**, *54*, 11169−11186.
(43) Islam, M. R.; Kang, N.; Bhanu, U.; Paudel, H. P.; Erementchouk, M.; Tetard, L.; Leuenberger, M. N.; Khondaker, S. I. Tuning the Electrical Property *Via* Defect Engineering of Single Layer MoS2 by Oxygen Plasma. *Nanoscale* **2014**, *6*, 10033−10039.
(44) Kang, N.; Paudel, H. P.; Leuenberger, M. N.; Tetard, L.; Khondaker, S. I. Photoluminescence Quenching in Single-Layer MoS2 *Via* Oxygen Plasma Treatment. *J. Phys. Chem. C* **2014**, *118*, 21258−21263.
(45) Choi, S.; Shaolin, Z.; Yang, W. Layer-Number-Dependent Work Function of MoS2 Nanoflakes. *J. Korean Phys. Soc.* **2014**, *64*, 1550−1555.
(46) Li, H.; Tsai, C.; Koh, A. L.; Cai, L.; Contryman, A. W.; Fragapane, A. H.; Zhao, J.; Han, H. S.; Manoharan, H. C.; Abild-Pedersen, F.; et al. Activating and Optimizing MoS2 Basal Planes for Hydrogen Evolution through the Formation of Strained Sulphur Vacancies. *Nat. Mater.* **2016**, *15*, 48−53.
(47) Zhou, W.; Zou, X.; Najmaei, S.; Liu, Z.; Shi, Y.; Kong, J.; Lou, J.; Ajayan, P. M.; Yakobson, B. I.; Idrobo, J.-C. Intrinsic Structural Defects in Monolayer Molybdenum Disulfide. *Nano Lett.* **2013**, *13*, 2615−2622.
(48) Jiménez Sandoval, S.; Yang, D.; Frindt, R. F.; Irwin, J. C. Raman Study and Lattice Dynamics of Single Molecular Layers of MoS_2. *Phys. Rev. B: Condens. Matter Mater. Phys.* **1991**, *44*, 3955−3962.
(49) Eda, G.; Yamaguchi, H.; Voiry, D.; Fujita, T.; Chen, M.; Chhowalla, M. Photoluminescence from Chemically Exfoliated MoS2. *Nano Lett.* **2011**, *11*, 5111−5116.
(50) Peng, B.; Lu, X.; Chen, S.; Huan, C. H. A.; Xiong, Q. H.; Mutlugun, E.; Demir, H. V.; Yu, S. F. Exciton Dynamics in Luminescent Carbon Nanodots: Electron−Hole Exchange Interaction. *Nano Res.* **2016**, *9*, 549−559.
(51) Liu, K. K.; Zhang, W. J.; Lee, Y. H.; Lin, Y. C.; Chang, M. T.; Su, C.; Chang, C. S.; Li, H.; Shi, Y. M.; Zhang, H.; et al. Growth of Large-Area and Highly Crystalline MoS2 Thin Layers on Insulating Substrates. *Nano Lett.* **2012**, *12*, 1538−1544.
(52) Zheng, J.; Zhang, H.; Dong, S.; Liu, Y.; Tai Nai, C.; Suk Shin, H.; Young Jeong, H.; Liu, B.; Loh, P. K. High Yield Exfoliation of Two-Dimensional Chalcogenides Using Sodium Naphthalenide. *Nat. Commun.* **2014**, *5*, 2995.
(53) Kong, D. S.; Wang, H. T.; Cha, J. J.; Pasta, M.; Koski, K. J.; Yao, J.; Cui, Y. Synthesis of MoS2 and MoSe2 Films with Vertically Aligned Layers. *Nano Lett.* **2013**, *13*, 1341−1347.
(54) Hangleiter, A. Nonradiative Recombination *Via* Deep Impurity Levels in Silicon: Experiment. *Phys. Rev. B: Condens. Matter Mater. Phys.* **1987**, *35*, 9149−9161.
(55) Kim, H.-S.; Lee, C.-R.; Im, J.-H.; Lee, K.-B.; Moehl, T.; Marchioro, A.; Moon, S.-J.; Humphry-Baker, R.; Yum, J.-H.; Moser, J. E.; et al. Lead Iodide Perovskite Sensitized All-Solid-State Submicron Thin Film Mesoscopic Solar Cell with Efficiency Exceeding 9%. *Sci. Rep.* **2012**, *2*, 591.
(56) Chen, W.; Wu, Y.; Yue, Y.; Liu, J.; Zhang, W.; Yang, X.; Chen, H.; Bi, E.; Ashraful, I.; Grätzel, M.; et al. Efficient and Stable Large-Area Perovskite Solar Cells with Inorganic Charge Extraction Layers. *Science* **2015**, *350*, 944−948.
(57) Lin, Y. C.; Zhang, W. J.; Huang, J. K.; Liu, K. K.; Lee, Y. H.; Liang, C. T.; Chu, C. W.; Li, L. J. Wafer-Scale MoS2 Thin Layers Prepared by Moo3 Sulfurization. *Nanoscale* **2012**, *4*, 6637−6641.
(58) Kang, K.; Xie, S.; Huang, L.; Han, Y.; Huang, P. Y.; Mak, K. F.; Kim, C.-J.; Muller, D.; Park, J. High-Mobility Three-Atom-Thick Semiconducting Films with Wafer-Scale Homogeneity. *Nature* **2015**, *520*, 656−660.
(59) Duesberg, G. S. Heterojunctions in 2d Semiconductors: A Perfect Match. *Nat. Mater.* **2014**, *13*, 1075−1076.
(60) Gao, L.; Ni, G. X.; Liu, Y.; Liu, B.; Castro Neto, A. H.; Loh, K. P. Face-to-Face Transfer of Wafer-Scale Graphene Films. *Nature* **2014**, *505*, 190−194.
(61) You, J.; Meng, L.; Song, T.-B.; Guo, T.-F.; Yang, Y.; Chang, W.-H.; Hong, Z.; Chen, H.; Zhou, H.; Chen, Q.; et al. Improved Air Stability of Perovskite Solar Cells *Via* Solution-Processed Metal Oxide Transport Layers. *Nat. Nanotechnol.* **2016**, *11*, 75−81.
(62) Qin, P.; Tanaka, S.; Ito, S.; Tetreault, N.; Manabe, K.; Nishino, H.; Nazeeruddin, M. K.; Grätzel, M. Inorganic Hole Conductor-Based Lead Halide Perovskite Solar Cells with 12.4% Conversion Efficiency. *Nat. Commun.* **2014**, *5*, 3834.
(63) Christians, J. A.; Fung, R. C. M.; Kamat, P. V. An Inorganic Hole Conductor for Organo-Lead Halide Perovskite Solar Cells. Improved Hole Conductivity with Copper Iodide. *J. Am. Chem. Soc.* **2014**, *136*, 758−764.
(64) Jeng, J. Y.; Chen, K. C.; Chiang, T. Y.; Lin, P. Y.; Tsai, T. D.; Chang, Y. C.; Guo, T. F.; Chen, P.; Wen, T. C.; Hsu, Y. J. Nickel Oxide Electrode Interlayer in CH3NH3PbI3 Perovskite/Pcbm Planar-Heterojunction Hybrid Solar Cells. *Adv. Mater.* **2014**, *26*, 4107−4113.
(65) Zhu, Z.; Bai, Y.; Zhang, T.; Liu, Z.; Long, X.; Wei, Z.; Wang, Z.; Zhang, L.; Wang, J.; Yan, F.; et al. High-Performance Hole-Extraction Layer of Sol−Gel-Processed Nio Nanocrystals for Inverted Planar Perovskite Solar Cells. *Angew. Chem., Int. Ed.* **2014**, *53*, 12571−12575.
(66) Etgar, L.; Gao, P.; Xue, Z.; Peng, Q.; Chandiran, A. K.; Liu, B.; Nazeeruddin, M. K.; Grätzel, M. Mesoscopic CH3NH3PbI3/TiO2 Heterojunction Solar Cells. *J. Am. Chem. Soc.* **2012**, *134*, 17396−17399.
(67) Nerngchamnong, N.; Yuan, L.; Qi, D.-C.; Li, J.; Thompson, D.; Nijhuis, C. A. The Role of Van Der Waals Forces in the Performance of Molecular Diodes. *Nat. Nanotechnol.* **2013**, *8*, 113−118.

DOI: 10.1021/acsnano.6b02845
ACS Nano 2016, 10, 6383−6391